Reactor Diameter Impact on Hot Zone Dynamics in an Adiabatic Packed Bed Reactor

Sandhya Sundarram, Ganesh A. Viswanathan, and Dan Luss
Dept. of Chemical and Biomolecular Engineering, University of Houston, Houston, TX 77204

DOI 10.1002/aic.11179
Published online April 26, 2007 in Wiley InterScience (www.interscience.wiley.com).

Recent analysis revealed that a pseudohomogeneous model of a uniformly active, adiabatic packed bed reactor can predict formation of stable hot zones in the cross-section of the reactor if the kinetic rate expression can lead to isothermal rate oscillations. This prediction was confirmed by simulations of CO oxidation. We show that hot zone formation in a shallow reactor can be predicted also for C_2H_4 hydrogenation, the kinetic model of which is structurally different from that of CO oxidation. Qualitatively different spatiotemporal temperature patterns may form under the same operating conditions. Their number increases as the reactor diameter is increased. An increase in the reactor diameter increases the time constant of the transversal heat dispersion and decreases the temperature synchronization among points on the same reactor cross-section. The interaction and conjugation among qualitatively different moving temperature patterns can lead to formation of complex motions. © 2007 American Institute of Chemical Engineers *AIChE J,* 53: 1578–1590, 2007
Keywords: packed-bed, transversal hot zone, adiabatic reactor, hydrogenation, spatiotemporal patterns

Introduction

Local transversal (normal to the flow direction) hot spots may form in the cross-section of packed-bed and trickle-bed reactors. Matros[1] observed hot zones formation in the cross-section of a packed-bed reactor in which the catalyst was not uniformly packed. Barkelew and Gambhir[2] reported formation of small clumps of molten catalyst (clinkers) during hydrodesulfurization in trickle bed reactors. Jaffe[3] reported that a local hot spot was formed by an obstruction to the flow in a hydrogenation trickle-bed reactor. Local moving hot spots (flickering) are known to form during ammonia oxidation and HCN synthesis in catalytic gauze convertors.[4] Local hot spots have also been reported during the regeneration of cordierite diesel particulate filters.[5] Transversal local hot regions have also been observed in various laboratory studies. Wicke and Onken[6,7] noted different temperatures at two locations in the same cross-section of a packed-bed reactor. Infrared imaging revealed local hot regions on the exterior surface of a radial flow reactor,[8–10] the top of shallow packed-bed reactors,[11–13] and a catalytic fiber cloth.[10,14] Sundarram et al.[15] found that global coupling between the effluents and the top of the reactor can affect the evolution, stability and shape of the temperature patterns.

Local hot zones may form in packed bed reactors when the catalyst has a nonuniform activity, when it is not packed uniformly,[1] or due to local obstructions to the flow.[3] In addition, hot spots may also form due to symmetry breaking in a uniformly active packed reactor.

Significant modeling effort has been directed to predict the formation of transversal (normal to the flow direction) hot zones in packed-bed reactors. Balakotaiah's research group[16,17] showed that when the flow rate is very low, convective instabilities may generate flow maldistribution, and hot zones in packed bed reactors. Similar predictions were made by Benneker et al.[18] Balakotaiah et al.[19,20] showed that

This article contains supplementary material available via the Internet at http://www.interscience.wiley.com/jpages/0001-1541/suppmat.

Current address of G. A. Viswanathan: Department of Neurology, Mount Sinai School of Medicine, One Gustave L. Levy Place, Box 1137, New York, NY 10029. E-mail: ganesh.viswanathan@mssm.edu
Correspondence concerning this article should be addressed to Dan Luss at dluss@uh.edu.

stationary transversal hot zones may form in an adiabatic packed bed reactor when the transversal effective heat conduction was lower than that of the species dispersion. However, as pointed out by Yakhnin and Menzinger,[21] the transversal effective heat dispersion in packed bed reactors is always larger than that of the species.

Viswanathan et al.[22] proved that transversal stationary temperature patterns are unstable when the local reaction rate in a uniform adiabatic packed bed reactor depends only on the surface concentration of a limiting reactant and temperature. Viswanathan and Luss[23] showed that transversal spatiotemporal hot zones may form when the local reaction rate may oscillate under constant ambient conditions. Marwaha and Luss[9] showed that various 2-dimensional temperature patterns may form on the surface of a thin, hollow cylindrical catalytic reactor used to carry out an oscillatory reaction. Sundarram and Luss[24] conducted two reactions in the same shallow packed-bed reactor. These experiments showed that the dynamics of the hot zones were mainly influenced by the reaction kinetics and not by the transport parameters.

An increase in the reactor diameter increases the ratio between the characteristic times for transversal heat dispersion to that of the reaction. This tends to decrease the synchronization between different locations on the cross-section. Thus, richer and more intricate patterns are expected to form as the system size is increased. The goal of our study is to investigate the impact of the reactor diameter on the patterns evolving in a shallow, uniform adiabatic packed bed reactor. Almost all previous studies of catalytic pattern formation were of oxidation reactions (mainly that of CO). We consider here the pattern evolution during the hydrogenation of ethylene, the rate expression for which is structurally different from that of the oxidation reaction.

The mechanism causing the temporal oscillation in the models of CO oxidation and ethylene hydrogenation are rather different. In the model of CO oxidation[23] the feedback between a reaction rate, that is strongly dependent on the surface coverage of oxygen, and its replenishment by adsorption causes a period transition between two limiting states. The oxygen surface concentration is high in one of the limiting states and low in the second. This mechanism can lead to isothermal oscillations.[25] In the C_2H_4 hydrogenation model the periodic behavior is due to the catalytic site blocking at a high temperature and subsequent site regeneration after cooling of the deactivated catalyst. This mechanism cannot lead to isothermal oscillations. These may occur only under nonisothermal operation. The frequencies and shape of the resulting spatial patterns are strongly dependent on the time constants of the dynamic variables.

Mathematical model

We study the formation of transversal (normal to the flow direction) local hot spots in an adiabatic packed bed reactor, in which the exothermic hydrogenation of ethylene is carried out, i.e.,

$$C_2H_4 + H_2 \rightarrow C_2H_6 \tag{1}$$

Following Bos and Westerterp,[26] we account for a periodic blocking activation of the Pd catalytic sites. The rate of the fractional blocking of the catalytic sites satisfies the relation:

$$\frac{\partial \Theta_{BL}}{\partial \tau} = Da_{BL}\mathbb{G}_1(\theta, \Theta_{BL}) - Da_{RE}\mathbb{G}_2(\theta, \Theta_{BL}) \tag{2}$$

where

$$\mathbb{G}_1(\theta, \Theta_{BL}) = \exp\left[\frac{\gamma_{BL}\theta}{1+\theta}\right](1-\Theta_{BL}),$$
$$\mathbb{G}_2(\theta, \Theta_{BL}) = \exp\left[\frac{\gamma_{RE}\theta}{1+\theta}\right]\Theta_{BL} \tag{3}$$

Θ_{BL} is the fraction of blocked sites and

$$\tau = \frac{vt}{d_p} \qquad \theta = \frac{T - T_{in}}{T_{in}}$$
$$\gamma_{BL} = \frac{E_{BL}}{\bar{R}T_{in}} \qquad \gamma_{RE} = \frac{E_{RE}}{\bar{R}T_{in}}$$
$$Da_{BL} = \frac{d_p}{v}k_{BL}(T_{in}) \quad Da_{RE} = \frac{d_p}{v}k_{RE}(T_{in}) \tag{4}$$

A pseudohomogenous model of a long, adiabatic packed-bed reactor is

$$\frac{\partial\theta}{\partial\tau} = \frac{1}{(Le)}\left[-\frac{\partial\theta}{\partial\eta} + \frac{1}{Pe_a^h}\frac{\partial^2\theta}{\partial\eta^2} + \frac{1}{Pe_\perp^h}\left\{\frac{1}{\xi}\frac{\partial}{\partial\xi}\left(\xi\frac{\partial\theta}{\partial\xi}\right) + \frac{1}{\xi^2}\frac{\partial^2\theta}{\partial\phi^2}\right\} + \beta\mathbb{R}(\theta, x, \Theta_{BL})\right] \tag{5}$$

$$\frac{\partial x}{\partial\tau} = \left[-\frac{\partial x}{\partial\eta} + \frac{1}{Pe_a^m}\frac{\partial^2 x}{\partial\eta^2} + \frac{1}{Pe_\perp^m}\left\{\frac{1}{\xi}\frac{\partial}{\partial\xi}\left(\xi\frac{\partial x}{\partial\xi}\right) + \frac{1}{\xi^2}\frac{\partial^2 x}{\partial\phi^2}\right\} + \mathbb{R}(\theta, x, \Theta_{BL})\right] \tag{6}$$

where we define

$$x = \frac{C_{in} - C}{C_{in}}, \quad \eta = \frac{z}{d_p}, \quad \xi = \frac{r}{R}, \quad \gamma = \frac{E}{\bar{R}T_{in}}, \quad Pe_a^h = \frac{vd_p(\rho C_p)_f}{\bar{\lambda}_a},$$
$$Pe_a^m = \frac{vd_p}{D_a}, \quad Pe_\perp^h = \left(\frac{R}{d_p}\right)^2 Pe_p^h, \quad Pe_\perp^m = \left(\frac{R}{d_p}\right)^2 Pe_p^m,$$
$$Da = \frac{d_p}{v}k(T_{in}), \quad \beta = \frac{(-\Delta H)C_{in}}{(\rho C_p)_f T_{in}}, \quad Le = \varepsilon + (1-\varepsilon)\frac{(\rho C_p)_s}{(\rho C_p)_f} \tag{7}$$

The dimensionless reaction rate is of first-order in hydrogen and zero-order in ethylene, i.e.,

$$\mathbb{R}(\theta, x, \Theta_{BL}) = Da\ \exp\left[\frac{\gamma\theta}{1+\theta}\right](1-x)(1-\Theta_{BL}) \tag{8}$$

The corresponding boundary conditions are

$$\frac{1}{Pe_a^h}\frac{\partial\theta}{\partial\eta} = \theta, \qquad \frac{1}{Pe_a^m}\frac{\partial x}{\partial\eta} = x, \qquad \eta = 0 \tag{9}$$

$$\frac{\partial\theta}{\partial\eta} = \frac{\partial x}{\partial\eta} = 0, \quad \eta = 1 \tag{10}$$

$$\frac{\partial\theta}{\partial\xi} = \frac{\partial x}{\partial\xi} = 0, \quad \xi = 1 \tag{11}$$

We denote by the symbol $\perp$ the effective species dispersion and heat dispersion in the transversal (normal to the flow)

direction. For reasons to be explained later, the characteristic length scale was selected to be d_p.

The finding of initial conditions that lead to stationary and oscillatory transversal temperature patterns in a packed bed reactor and the corresponding dynamic simulations are very demanding tasks. Thus, to gain insight into the formation and structure of the various possible, stationary and oscillatory nonuniform states, and their dependence on the reactor diameter, we first studied a simplified version of the full model, namely that of a shallow reactor. That model is obtained by a Liapunov–Schmidt reduction of the long reactor model.[27] This procedure has previously been used by Balakotaiah et al.[28] and Viswanathan and Luss[22] and details of it are described by Viswanathan.[29]

A Liapunov–Schmidt reduction of Eqs 5, 6, and 8–10 yields the pseudohomogeneous *shallow* reactor model

$$\frac{\partial\theta}{\partial\tau}=\frac{1}{(Le)}\left[\frac{1}{Pe_{\perp}^{h}}\left\{\frac{1}{\xi}\frac{\partial}{\partial\xi}\left(\xi\frac{\partial\theta}{\partial\xi}\right)+\frac{1}{\xi^2}\frac{\partial^2\theta}{\partial\phi^2}\right\}-\theta+\beta\mathbb{R}(\theta,x,\Theta_{BL})\right] \tag{12}$$

$$\frac{\partial x}{\partial\tau}=\frac{1}{Pe_{\perp}^{m}}\left\{\frac{1}{\xi}\frac{\partial}{\partial\xi}\left(\xi\frac{\partial x}{\partial\xi}\right)+\frac{1}{\xi^2}\frac{\partial^2 x}{\partial\phi^2}\right\}-x+\mathbb{R}(\theta,x,\Theta_{BL}) \tag{13}$$

where Θ_{BL} and $\mathbb{R}$ satisfy Eqs. 2 and 8. The axial averaged conversion and dimensionless temperature are denoted as

$$\theta=\int_0^1\theta\,d\eta,\quad x=\int_0^1 x\,d\eta \tag{14}$$

The corresponding boundary conditions are

$$\frac{\partial\theta}{\partial\xi}=\frac{\partial x}{\partial\xi}=0,\quad \xi=1 \tag{15}$$

and the transversal mass and heat Peclet numbers are $Pe_{\perp}^{m}=Pe_{p}^{m}(R/d_p)^2$ and $Pe_{\perp}^{h}=Pe_{p}^{h}(R/d_p)^2$. In all our simulations, we assigned the particle Peclet numbers the values of $Pe_{p}^{m}=5$ and $Pe_{p}^{h}=1$.

The simulations of the shallow reactor model were performed by discretizing the polar coordinates using a second-order central finite difference scheme. In order to circumvent the singularity at the center of the cylindrical reactor ($\xi=0$), the grid points were placed at $\xi_j=\frac{(2j-1)}{(2N-1)}\ \forall j=1,N$.[30] The discretized model is similar to a cell model in a circular cross-section, with the dispersion terms mimicked by exchange coefficients among the cells. The dynamic simulations were carried out using LIMEX (linear implicit extrapolator).[31,32] The numerical simulations of angularly uniform cases were carried out using a direct solver (LAPACK), while a sparse iterative solver (GMRES/BiCGSTAB) was used in the two-dimensional simulations. The sparse iterative solver usually converged in two or three iterations in the linear step. The steady-state solutions were computed by a Newton–Raphson iteration procedure using a nonlinear equation solver (NLEQ).[33] The bifurcation diagrams were computed using pseudoarc length continuation scheme.[34]

Linear stability analysis

The transversally uniform steady-state solution of the shallow reactor model (Eqs. 2, 12, 13, and 15) is obtained by deleting the time derivatives and the spatial derivatives in the radial and the azimuthal directions from Eqs. 12 and 13. A uniform steady-state solution $u_{ss}=(\theta,\ x,\ \Theta_{BL})_{ss}$ is stable with respect to homogeneous perturbations if and only if all the eigenvalues of the Jacobian

$$\mathbb{L}=\begin{bmatrix}(-1+\beta\mathbb{R}_\theta)/Le & \beta\mathbb{R}_x/Le & \beta\mathbb{R}_{\Theta_{BL}}/Le\\ \mathbb{R}_\theta & -1+\mathbb{R}_x & \mathbb{R}_{\Theta_{BL}}\\ Da_{BL}\mathbb{G}_{1\theta}-Da_{RE}\mathbb{G}_{2\theta} & 0 & Da_{BL}\mathbb{G}_{1\Theta_{BL}}-Da_{RE}\mathbb{G}_{2\Theta_{BL}}\end{bmatrix}\Bigg|_{u_{ss}} \tag{16}$$

have a negative real part. The first partial derivatives of the rates are:

$$\begin{aligned}&\mathbb{R}_\theta=\partial\mathbb{R}/\partial\theta\quad \mathbb{R}_x=\partial\mathbb{R}/\partial x\quad \mathbb{R}_{\Theta_{BL}}=\partial\mathbb{R}/\partial\Theta_{BL}\\ &\mathbb{G}_{1\theta}=\partial\mathbb{G}_1/\partial\theta\quad \mathbb{G}_{1\Theta_{BL}}=\partial\mathbb{G}_1/\partial\Theta_{BL}\quad \mathbb{G}_{2\theta}=\partial\mathbb{G}_2/\partial\theta\\ &\mathbb{G}_{2\Theta_{BL}}=\partial\mathbb{G}_1/\partial\Theta_{BL}\end{aligned} \tag{17}$$

A Hopf bifurcation from a stable uniform solution that leads to homogeneous oscillations exists when the condition

$$\begin{aligned}\det(\mathbb{L})=&\left[-1+\mathbb{R}_x-\frac{1}{Le}+\frac{\beta\mathbb{R}_\theta}{Le}+Da_{BL}\mathbb{G}_{1\Theta_{BL}}-Da_{RE}\mathbb{G}_{2\Theta_{BL}}\right]\\ &\times\left[\frac{1}{Le}(1-\mathbb{R}_x-\beta\mathbb{R}_\theta)-\det(\mathbb{L})\right.\\ &\left.+(Da_{BL}\mathbb{G}_{1\Theta_{BL}}-Da_{RE}\mathbb{G}_{2\Theta_{BL}})\left(-1+\mathbb{R}_x-\frac{\mathbb{R}_x}{Le}\right)\right]\end{aligned} \tag{18}$$

is satisfied, as is explained in Appendix A.

To determine the conditions leading to evolution of transversal patterns we check the stability of the uniform solutions with respect to nonhomogenous perturbations of the form

$$\boldsymbol{\omega}_{mn}(\xi,\phi)=\boldsymbol{\omega}\cdot J_m(\mu_{mn}\xi)\cdot e^{im\phi} \tag{19}$$

where m and n are the radial and azimuthal mode numbers. μ_{mn} satisfies the relation

$$\left.\frac{dJ_m(\mu_{mn}\xi)}{d\xi}\right|_{\xi=1}=mJ_m(\mu_{mn})-\mu_{mn}J_{m+1}(\mu_{mn})=0 \tag{20}$$

and J_m and $e^{im\phi}$ are the radial and angular eigenfunctions. The Bessel function of the first kind, J_m is real due to the adiabatic (no-flux) boundary conditions.[35] The first nine values of μ_{mn} are reported in Table 1.[23] The uniform solution becomes unstable to a nonhomogeneous perturbation at either a stationary or an oscillatory neutral stability point.

An $\mathbb{O}(2)$ symmetry-breaking bifurcation from a uniform solution leading to stationary transversal nonuniform states can occur at a stationary neutral stability point, when the

Table 1. First Nine Eigenvalues Satisfying Eq. 20

No.	m	n	μ_{mn}
1	1	1	1.8412
2	2	1	3.0542
3	0	1	3.8317
4	3	1	4.2012
5	4	1	5.3176
6	1	2	5.3314
7	5	1	6.4156
8	2	2	6.7061
9	0	2	7.0155

nonhomogeneously perturbed Jacobian ($\mathbb{L}-\mathbb{P}$) has a zero eigenvalue, i.e., $\det(\mathbb{L}-\mathbb{P}) = 0$, where

$$\mathbb{P} = \begin{bmatrix} \frac{1}{Le}\left(\frac{\mu_{mn}^2}{Pe_{\perp}^{h}}\right) & 0 & 0 \\ 0 & \left(\frac{\mu_{mn}^2}{Pe_{\perp}^{m}}\right) & 0 \\ 0 & 0 & 0 \end{bmatrix} \tag{21}$$

We prove in Appendix B that such a bifurcation cannot occur from a stable uniform state for a practical range of parameters. A bifurcation from unstable uniform state leads to an unstable nonuniform state.

An $\mathbb{O}(2)$ symmetry-breaking Hopf bifurcation leading to a transition from a uniform steady state to a spatiotemporal pattern can occur at an oscillatory neutral stability point, at which the perturbed Jacobian ($\mathbb{L}-\mathbb{P}$) has a pair of imaginary eigenvalues. At such a neutral stability point the steady state equations (Eqs. 2, 12, 13) and the complex eigenvalue problem

$$[\mathbb{L} - \mathbb{P}] \cdot (\boldsymbol{\omega}_r \pm i\boldsymbol{\omega}_i) = \pm i\sigma(\boldsymbol{\omega}_r \pm i\boldsymbol{\omega}_i) \tag{22}$$

are satisfied, where σ is the coefficient of the imaginary eigenvalue, and $\boldsymbol{\omega} = \boldsymbol{\omega}_r \pm i\boldsymbol{\omega}_i$ are the corresponding complex eigenvectors. Separating the real and imaginary parts, an oscillatory neutral stability point is obtained by simultaneously solving the set of equations:

$$\mathbb{F}(u_{ss}, Da) = 0 \tag{23}$$

$$[\mathbb{L} - \mathbb{P}] \cdot \boldsymbol{\omega}_r + \sigma\boldsymbol{\omega}_i = 0 \tag{24}$$

$$[\mathbb{L} - \mathbb{P}] \cdot \boldsymbol{\omega}_i - \sigma\boldsymbol{\omega}_r = 0 \tag{25}$$

$$\|\boldsymbol{\omega}_r\| + \|\boldsymbol{\omega}_i\| - 1 = 0 \tag{26}$$

$$\boldsymbol{\omega}_r \cdot \boldsymbol{\omega}_i = 0 \tag{27}$$

where Eqs. 26 and 27 are the nontriviality conditions. The oscillatory neutral stability curve, that is the locus of these points, bounds the parameter space in which nonuniform transversal states may exist.

The contribution of the transversal dispersion term, $\mathbb{P}$, in the eigenvalue problem (Eqs. 24 and 25) becomes insignificant when $Pe_{\perp}$ is very large. At large values of R/d_p, $Pe_{\perp}$ is very large and consequently the oscillatory neutral stability points approach the Hopf bifurcation points (due to homogeneous perturbations) of the uniform steady state. Thus, to compute the locus of the oscillatory neutral stability points, we start from conditions at which the uniform state has a Hopf bifurcation. A pseudoarc length continuation scheme (with R/d_p as the continuation parameter) is then used to construct the oscillatory neutral stability curves for various mode numbers, μ_{mn}. A perturbation of a steady state close to the neutral stability point by the eigenmode is an initial condition that may lead to the evolution of transversal hot zones.

All the numerical simulations were performed for the set of parameters:

$$Le = 1416, \quad \gamma_{BL} = 7.7, \quad \gamma_{RE} = 0.77, \quad \beta = 0.95,$$
$$\gamma = 15, \; Da_{RE} = 1e-5, \quad Da_{BL} = 3e-5 \tag{28}$$

Figure 1a is the bifurcation diagram of the dimensionless temperature of the uniform steady states versus Da. The corresponding root loci of the leading pair of complex eigenvalues are shown in Figures 1b,c. A pair of complex eigenvalues emerges at points A and C (in Figure 1) and become real at points B and D. The complex eigenvalues cross the imaginary axis at H_1 and H_2 (Figure 1a) leading to two Hopf bifurcations (due to homogeneous perturbations) from unique steady-state solutions. H_1 is on the branch of low-temperature states while H_2 is on that of the high-temperature states. All the uniform steady states between H_1 and H_2 are unstable to homogeneous perturbations. The limit cycles in Figure 1a are represented by the maximum oscillatory temperature (open circles), computed by dynamic simulations. The simulations suggest that both H_1 and H_2 are subcritical. The coefficient of the imaginary eigenvalue (σ) at the Hopf bifurcation points, H_1 and H_2 is 0.0001255 and 0.0001842, respectively. The corresponding oscillation period next to the bifurcation point of ($2\pi/\sigma$) is 50065 and 34148, respectively.

The neutral stability curve was computed by continuation with respect to R/d_p using Da as the distinguished parameter. (The perturbed Jacobian, ($\mathbb{L}-\mathbb{P}$) has a pair of imaginary eigenvalues at all the points along each curve.) For the sake of simplicity, oscillatory neutral stability curves for the first three transversal eigenmodes are presented in the plane of R/d_p versus θ in Figure 2b. (The neutral stability curves in the (R/d_p, Da) plane is presented as the supplementary information Figure S1.) Figure 2a describes the corresponding eigenmodes. The neutral stability curves have the shape of a cup that is bounded between the two Hopf bifurcation points and therefore encompass the limit points. The neutral stability curves of the higher modes are nested within those of the lower modes.

Spatiotemporal patterns

The existence and finding of spatiotemporal patterns requires information on the system parameters for which they exist, and of initial conditions that are in the domain of attraction of the pattern of interest. To find a specific moving pattern, we followed the procedure used by Viswanathan and Luss.[23] We start by constructing the neutral stability curve for the specific mode (m and n values) in the R/d_p vs. Da plane for that mode. To obtain a corresponding nonuniform state, we then choose a point within that region close to the neutral stability boundary, and conduct dynamic simulations using as initial conditions (nonhomogeneous perturbation)

$$u = u_{ss} + A\boldsymbol{\omega}_r J_m(\mu_{m,n}\xi)e^{im\phi} \tag{29}$$

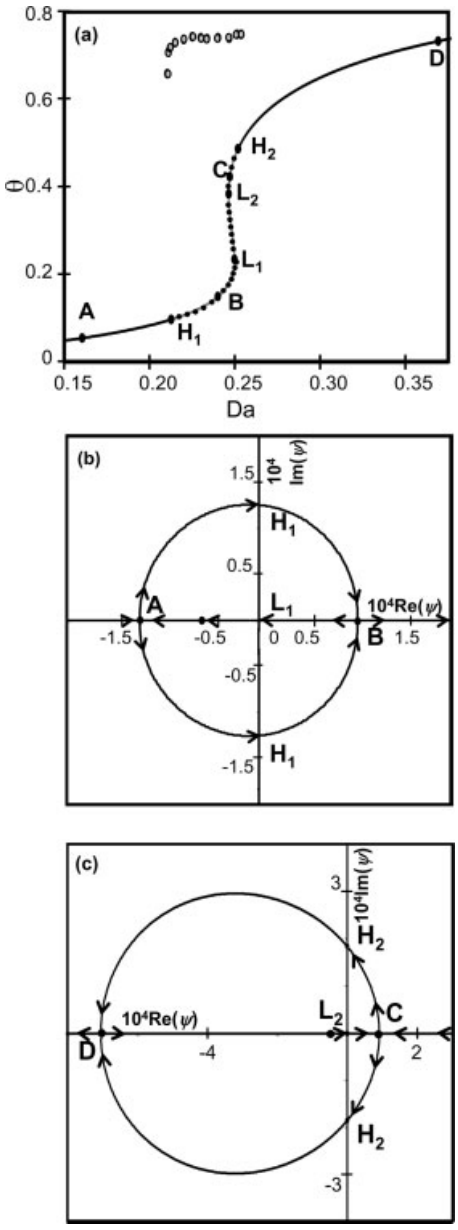

Figure 1. (a) The bifurcation diagram of the dimensionless temperature of the uniform steady states versus *Da*; (b) root locus of the leading pair of complex eigenvalues emerging at A which become real at B; (c) root locus of the leading pair of complex eigenvalues emerging at C which become real at D.

with A in [0.05, 0.5]. The proper range of A values for each case was determined by conducting the simulations for several A values. Perturbations in the values of R/d_p and Da were then used to obtain the nonuniform state for other R/d_p and Da values. Several different types of spatiotemporal patterns corresponding to different modes (specified by $J_m(\mu_{mn}\xi)e^{im\phi}$ in Eq. 29) may be obtained for the same set of system parameters by the use of different initial conditions. We restricted our computations for the perturbation of the homogenous steady state by modes with m varying from 0 to 2 and $n = 1$, i.e., to the first three transversal modes.

The simulations with perturbations corresponding to the first ($m = 1$, $n = 1$), second ($m = 2$, $n = 1$), and third ($m = 0$, $n = 1$) modes generated a band, antiphase and target motion, respectively. Simulations were conducted for several R/d_p values. We present here results for R/d_p of 100 (some simulations for $R/d_p = 58$ are presented in the supplementary information).

We investigated the impact of the ratio between the characteristic time constant for the transversal thermal dispersion to that of the chemical reaction, which is

$$\frac{t_{R1}}{t_R} = Da\ Pe_p^h \left(\frac{R}{d_p}\right)^2 \tag{30}$$

on the synchronization of the pattern in the cross-section. Clearly, the larger R/d_p, the higher is the probability that patterns corresponding to different modes will exist on the same cross-section, and that mode interactions will generate patterns different from any of the pure modes. In order to detect this, we define two types of spatiotemporal motions: simple and complex motions. Note that due to the rotational symmetry of the $\mathbb{O}(2)$ symmetry group, every (simple or complex) solution can be rotated by a certain azimuthal angle to obtain a new solution.

A simple motion is one that preserves the qualitative features of the initial nonhomogeneous mode perturbation (Eq. 19) that generates the motion. In the case of target motion, which is azimuthally uniform, the simple motion can be either inwards or outwards. To obtain a simple motion, we

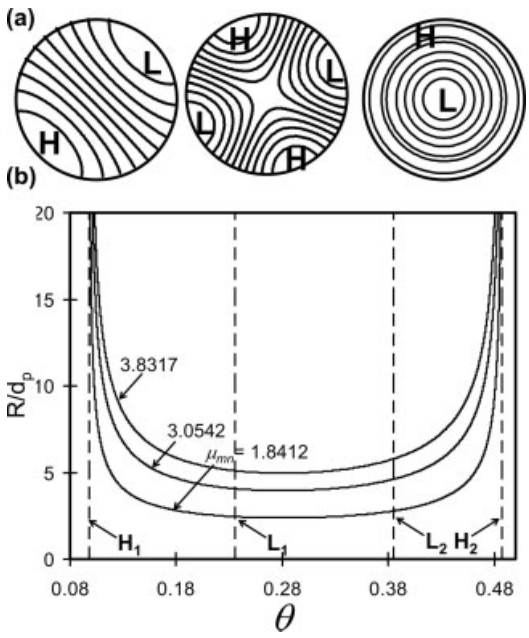

Figure 2. (a) The first three transversal eigenmodes for mode number with $m = 0, 1, 2$ and $n = 1$, (b) their respective neutral stability curves in the R/d_p vs. θ plane.

(Corresponding neutral stability curve in R/d_p vs. Da plane is in supplementary information, Figure S1.)

selected parameters close to the neutral stability point for an R/d_p of interest and gradually perturbed Da by about $\sim 10^{-3}$ during successive dynamic simulations, while maintaining the qualitative feature of the motion till reaching the desired Da. A complex motion contains the qualitative features of several transversal modes or some conjugation of features of several modes. Complex motions were obtained by a large parameter (R/d_p, Da) perturbation of the uniform state by one of the modes. The spatiotemporal simple and complex patterns in Figures 3–10 are all computed with a Da of 0.25.

It is extremely difficult to identify the qualitative features of the spatiotemporal motion by inspection. This task can be simplified by using principal component analysis (PCA) to decompose the spatiotemporal patterns into orthogonal time-independent spatial modes (or principal modes) and time-dependent amplitudes.[36] PCA provides an objective characterization of the underlying dynamics in space and time. It has been successfully applied to the analysis of spatiotemporal patterns on catalytic surfaces[13,37] and the details are presented by Graham et al.[37] In this procedure, the spatiotemporal data $\boldsymbol{u}(\xi,\phi,\tau)$ are represented by the series

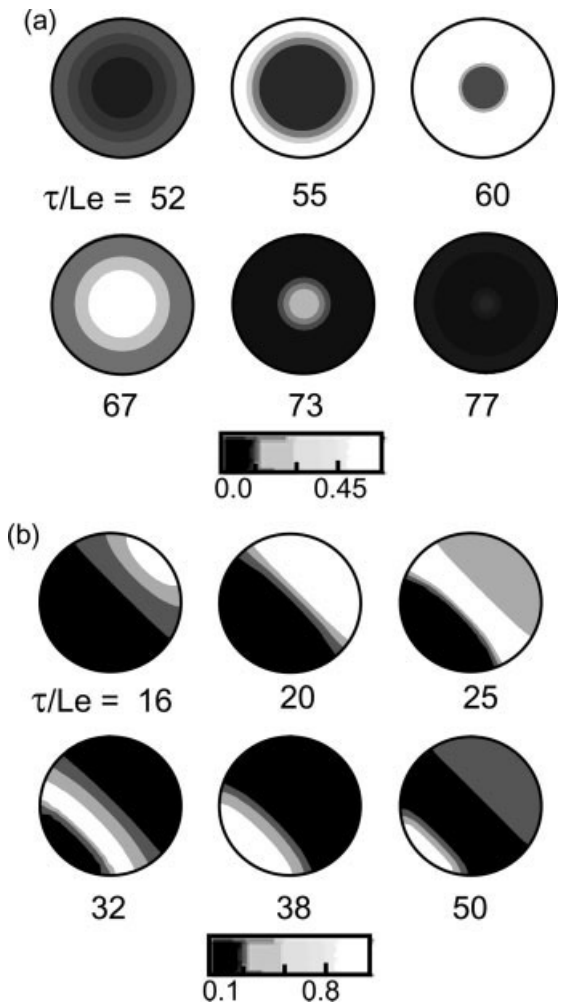

Figure 3. Snapshots of simple motion at R/d_p = 100: (a) inwards target motion and (b) band motion.

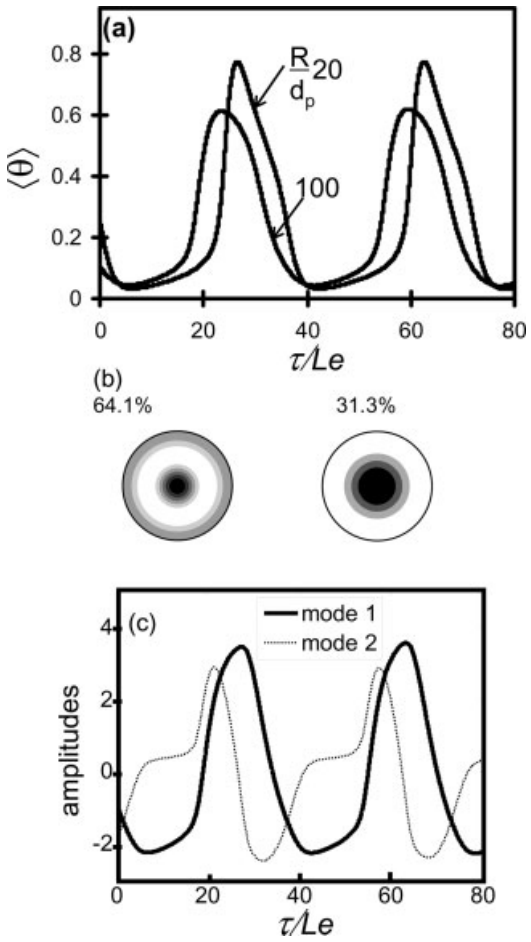

Figure 4. (a) Time series of simple target motions at R/d_p = 20 and 100, (b) first two POD modes of the target motion described in Figure 3a with their energy fractions (%), (c) time series of the POD modes.

$$\boldsymbol{u}(\xi,\phi,\tau) = \sum_{i=1}^{N} \mathcal{A}_i(\tau)\varphi_i(\xi,\phi) \tag{31}$$

where $\mathcal{A}_i(\tau)$ are orthogonal time-dependent amplitudes and $\varphi_i(\xi, \phi)$ spatial modes. Thus,

$$\left\langle \varphi_i(\xi,\phi)\cdot\varphi_j(\xi,\phi)\right\rangle = \delta_{ij} \tag{32}$$

$$\overline{\mathcal{A}_i(\tau)\mathcal{A}_j(\tau)} = \lambda_i\delta_{ij} \tag{33}$$

where λ_i represent the energy captured by the principal modes, which correspond the relative contribution of the principal modes to the overall motion. We used the PCA routine in MATLAB to conduct this analysis.[38]

Figure 3 shows snapshots of two different simple motions—band and targets, at various instances during one cycle. (Note that the dimensionless time is scaled with Le.) The corresponding time series of the effluent temperature and of the first two principal modes are presented in Figures 4 and 5. Simulations were conducted using as initial conditions two complementary types of azimuthally symmetric target

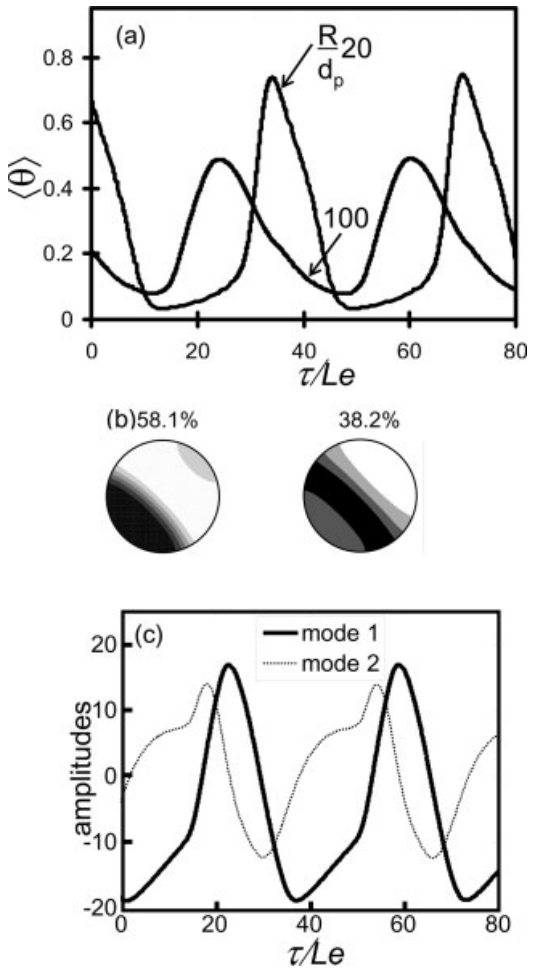

Figure 5. (a) Time series of simple band motion at R/d_p = 20 and 100, (b) first two POD modes of the band motion described in Figure 3b with their energy fractions (%), (c) time series of the POD modes.

mode. One in which the lowest initial temperature was at the center and increased with radial distance (type I) and one in which the highest temperature was at the center and decreased with radial distance (type II). For $R/d_p = 20$ (snapshots not shown) both initial conditions led to outward moving targets wherein, during the rising (receding) part of the cycle, a ring of hot (cold) temperature emerged at the center, expanded and captured the whole cross-section. For $R/d_p = 58$, a simple inward targets motion was obtained for the initial conditions of type I, while outward moving targets was obtained by type II initial conditions. (Snapshots of these motions are included as Figure S2 in the supplementary information.) For $R/d_p = 100$, both simple inward and outward moving targets were obtained. We present only the inward moving targets in Figure 3a. The time series in Figure 4a reveal that the maximum effluent temperature decreases with the increase in the reactor diameter. (The values of τ/Le in Figure 4a correspond to those in Figure 3a) The spatial profiles of the corresponding first two principal components (snapshots in Figure 4b) reveal that the principal modes are qualitatively similar to those of the third transversal mode used as the initial perturbation. Further, the first two modes capture almost all the energy of the motion.

Snapshots of the simple band motion simulated for $R/d_p = 100$ are shown in Figure 3b for various instances in a cycle. The effluent temperature time series for the simple motion at $R/d_p = 20$ (snapshots not shown) and 100 are shown in Figure 5a. During every periodic simple band motion, a hot (cold) zone emerged at a wall during the rising (receding) part of the cycle. It then traversed across the cross-section and exited on the other side. The peak effluent temperature during the band motion was lower than those observed during the moving targets. Similarly, simple antiphase motion (snapshots not shown) was obtained for R/d_p of 20–35 wherein two hot (cold) zones emerged at the diametrically opposite ends during the rising (receding) part of the cycle. The two zones then merged and exited the reactor at positions perpendicular to those at which they emerged.

Snapshots of complex targets, band and antiphase motions for $R/d_p = 100$ are presented in Figures 6a, 7a, and 8a, respectively. The corresponding first two principal components with their energy contributions are illustrated in Figures 6b, 7b, and 8b, respectively. The corresponding time series of the dynamic motions as well as those of the first two prin-

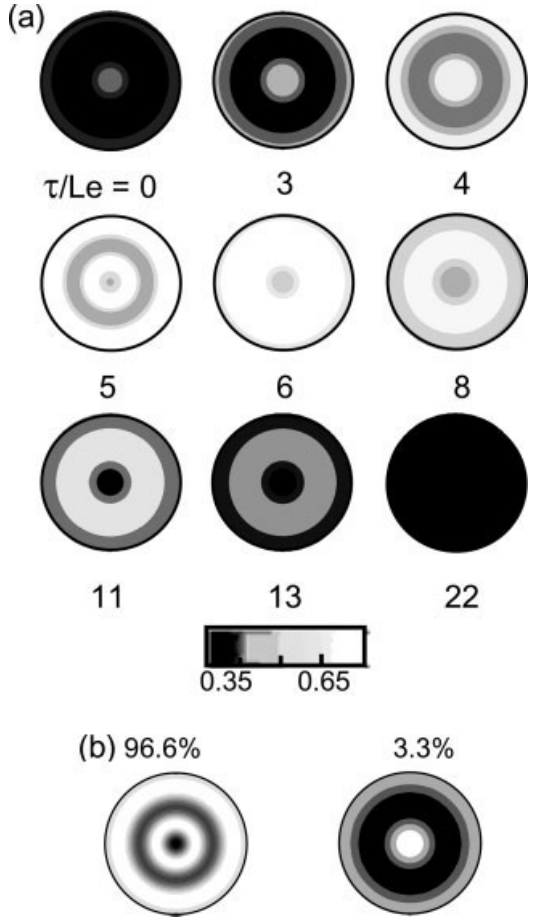

Figure 6. (a) Snapshots of complex—both inward and outward moving—target motion at R/d_p = 100 and (b) corresponding POD modes with the energy fractions.

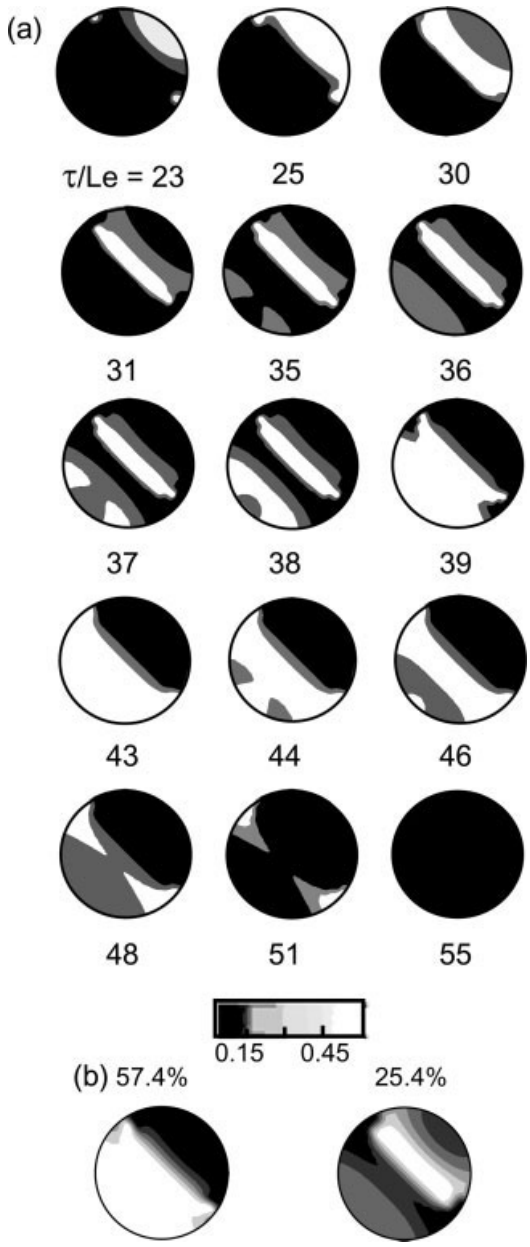

Figure 7. (a) Snapshots of complex band motion at R/d_p = 100 and (b) corresponding POD modes with the energy fractions.

cipal components are shown in Figures 9 and 10. The complex target pattern motion consisted of several hot and cold rings. For example, the case shown in Figure 6a, consisted of simultaneous formation of a hot ring at both the surface and the center (Figure 6a, $\tau/Le = 4$). These two hot zones moved in opposite directions. The outer ring moved inwards and the inner hot ring outwards. Eventually the two hot rings collided and conquered almost the whole surface ($\tau/Le = 6$). This was followed by cooling and formation of a cold (dark) ring next to the wall and a cold circular region in the center ($\tau/Le = 11$). The two cold zones moved towards each other, and eventually collided and conquered the whole surface ($\tau/Le = 22$). The maximum effluent temperature during the complex targets motion (about 0.75, Figure 9) was higher than that attained during simple targets motion (about 0.6, Figure 4a) at the same Da. The decomposition of the motion by PCA shows that the first component (Figure 6b) consists of two cold zones and three hot zones, whereas the second has one cold and two hot zones. A comparison of these principal components with those in the case of simple motion (Figure 4b) suggests that higher modes contributed to the complex target motion. (Note that the principal components of the simple motion for the same set of parameters were qualitatively similar to the perturbing mode.)

A (very) complex band motion was obtained at $R/d_p = 100$, as shown by Figure 7a. Initially a large hot temperature pulse and two smaller pulses emerged on the reactor sur-

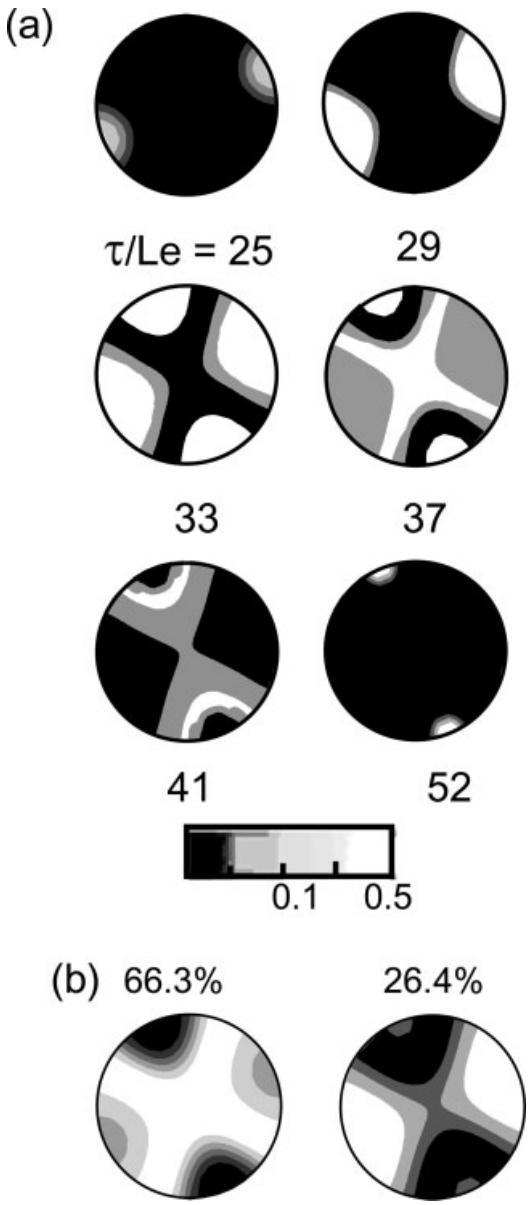

Figure 8. (a) Snapshots of complex antiphase motion at R/d_p = 100 and (b) corresponding POD modes with the energy fractions.

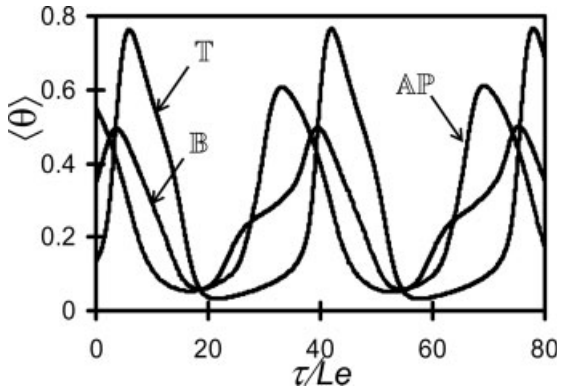

Figure 9. Time series of complex motions at R/d_p of 100, $\mathbb{T}$ – targets, $\mathbb{B}$ – band, $\mathbb{AP}$ – antiphase.

face (τ/Le =23). They coalesced, grew, and formed a band which traveled towards the center. The hot band was fully surrounded by adjacent cold regions (τ/Le =31), a novel feature that did not occur for smaller reactor diameters. Two (symmetric) hot zones formed then on the diametrically opposite side of the reactor, grew and formed a second high-temperature band. The two hot bands moved towards each other, collided, and formed a large hot zone (τ/Le = 43). Next, two cold zones formed (τ/Le = 44), grew to a band and formed a low temperature band (τ/Le = 46). The two cold zones moved towards each other, coalesced and occupied the whole surface at τ/Le =55. A comparison of the first two principal modes (Figure 7b) with those of the simple motion (Figure 5b) obtained for the same set of parameters suggests the conjugation of several modes in this complex motion.

An intricate antiphase motion was observed at R/d_p =100 (Figure 8a). The snapshots show that a pair of hot zones, emerged at diametrically opposite locations of the reactor wall and moved towards the center (τ/Le = 29). Then another pair of diametrically opposite hot zone formed in a direction perpendicular to that of the former pair. The expansion of these four hot zones led to the formation of an 'X'-shaped cold zone surrounded by hot zones (τ/Le = 33). The collision of the hot zones broke up the cold X and pushed the cold zones towards the surface. Next, a pair of cold zones emerged at diametrically opposite locations of the reactor wall and moved towards the center (τ/Le = 37). While the cold zones moved towards the center, another pair of (diametrically opposite) cold zones (τ/Le = 41) appeared and as a result, four cold zones encapsulated the hot zones. At the end of the cycle, the cold zones capture the whole surface (τ/Le = 52). The first two principal modes (Figure 8b) resemble the fifth and second transversal eigenmodes. These two modes captured significant (66.4% and 26.4%) fraction, but not most of the energy associated with the motion. This suggests the involvement of the higher modes in this complex motion as well.

Conclusions and Discussion

The simulations of a pseudohomogeneous model of a shallow, adiabatic uniform packed-bed reactor revealed that a rich variety of qualitatively different stable spatiotemporal transversal temperature patterns may form during the hydrogenation of the ethylene. An $\mathbb{O}(2)$ symmetry-breaking Hopf bifurcation led to the formation of the stable spatiotemporal hot zones. The kinetic model of ethylene hydrogenation of Bos and Westerterp[26] that accounts for a periodic blocking-activation of the Pd catalytic sites is structurally very different form that of CO oxidation that has been used in most previous studies of pattern formation in packed-bed reactors. The current study corroborates the prediction of Viswanathan and Luss[23] that kinetic models having oscillatory features can lead to prediction of stable spatiotemporal pattern formation in pseudohomogeneous models of packed-bed reactors.

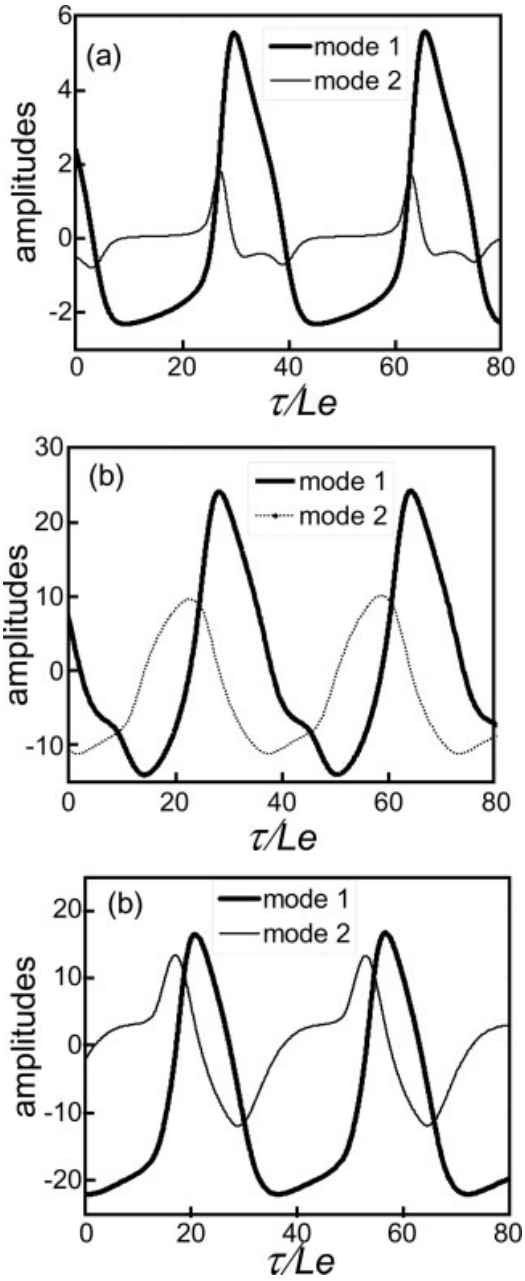

Figure 10. Time series of first two POD modes of (a) motion depicted in Figure 6, (b) motion in Figure 7, and (c) motion in Figure 8.

The analysis and simulations showed that use of different initial conditions can lead to formation of qualitatively different types of spatiotemporal hot zones. The larger the diameter of the reactor, the larger is the number of different modes that may lead to bifurcation to nonuniform states. The simulations showed that in addition to simple patterns (the spatial features of which resemble those of the eigenmodes used as the initial perturbation of the homogeneous steady state), complex motions, which differ from those of the initial perturbation, may form. The dynamic features of the complex motion are much more intricate than those for simple motion (Figure 3) obtained for the same set of parameters. The dynamic features illustrated in Figures 6–8 for $R/d_p = 100$ are much more intricate than those of the three transversal eigenmodes used to generate the band, antiphase, and target patterns next to the corresponding neutral stability curves. A comparison of the amplitudes and modes of the first two principal components during the complex motion at R/d_p of 100 (Figure 6) with those of the simple motion suggests that the intricate dynamics features during complex motion are generated by a conjugation among several modes.

The simulations showed that the dynamic features of the patterns generated for R/d_p values close to the minimum of the neutral stability curves were very similar to those of the eigenmodes used as initial perturbations of the uniform states. However, complex motion tended to form when the reactor diameter increased above a threshold value. This occurs as the time constant for transversal heat dispersion is proportional to $(R/d_p)^2$, while that of the reaction does not depend on the reactor diameter. Thus, an increase in the reactor diameter increases the ratio between the time constant of the transversal heat dispersion relative to that of the reaction. This, in turn, decreases the synchronization among various points on the surface and leads to complex mixed mode motions and conjugation. The evolution of complex motion at larger reactor diameters resembles the formation of a characteristic pattern size in homogenous reaction–diffusion systems.[39]

The key to a systematic finding of the various transversal temperature patterns is the construction of the oscillatory neutral stability curves and use of the corresponding eigenmodes as initial conditions that lead to spatiotemporal hot zones. The construction of the oscillatory neutral stability curves is rather simple for the adiabatic reactor as the no-flux boundary conditions enable use of the same transversal eigenmodes (Bessel functions of first kind and exponentials) for both the temperature and conversion variables. A reactor model that accounts for heat loss at the surface has different boundary conditions for the temperature and conversion variables and therefore requires a much more intricate analysis which uses two different Bessel functions.

Viswanathan et al.[22] proved that a pseudohomogeneous model cannot predict a symmetry-breaking bifurcation to a stable, stationary, transversal nonuniform states in a shallow, adiabatic reactor under the practical condition that the heat dispersion exceeds that of the species. This conclusion was proven for reactions whose rate depends only on the temperature and surface concentration of the limiting reactant. We show in the appendix that a symmetry-breaking bifurcation from a stable uniform steady state to a stable, stationary, transversal nonuniform state cannot be generated using the periodic blocking-activation kinetic model. This leaves open the question which, if any, kinetic models can predict the formation of stationary nonuniform states in shallow, uniformly active packed-bed reactors.

We wish to point out that this study is concerned with the possible formation and features of hot zones using a model of a reactor uniformly packed with uniformly active catalyst, which does not consider any changes in the physical properties or velocity. In practice, hot zones may form due to either differences in the activity of different catalytic pellets, flow maldistribution due to nonuniform packing or variations in physical properties with temperature and conversion. We did not consider any of these effects as our goal was to determine the possible formation of these hot zones due to symmetry breaking in a uniformly active packed bed reactor and the impact of reactor diameter.

Acknowledgments

We wish to thank the BSF, NSF and the ACS-PRF, for their support of this research, and the San Diego Supercomputing Center and the Department of Mathematics, University of Houston for use of their facilities. We are thankful to Martin Golubitsky for helpful discussions and advice.

Notation

A = constant coefficient for initial conditions in Eq. 28
C = concentration (mol m^{-3})
C_p = specific heat capacity (J kg^{-1} K^{-1})
D = species diffusion coefficient (m^2 s^{-1})
Da = Damkohler number
d_p = diameter of particle (m)
E = activation energy (J mol^{-1})
$\mathbb{F}$ = vector of steady state equations
$\mathbb{G}_1$ = rate of blocking of active sites
$\mathbb{G}_2$ = rate of reactivation of active sites
$\mathbb{I}$ = identity matrix
J = Bessel function of the first kind
k = intrinsic reaction rate constant (s^{-1})
L = reactor length (m)
$\mathbb{L}$ = first Fréchet derivative
Le = Lewis number (defined by Eq. 11)
N = radial grid points
$\mathbb{P}$ = transversal perturbation matrix (defined by Eq. 22)
Pe = Peclet number (defined by Eq. 11)
Pe_p^b = transversal particle heat Peclet number ($vd_p/(\bar{\lambda}_\perp/(\rho C_p)_f)$)
Pe_p^m = transversal particle mass Peclet number ($vd_p/\bar{D}_\perp$)
r = radial coordinate (m)
R = reactor radius (m)
$\overline{R}$ = universal gas constant (J mol^{-1} K^{-1})
$\mathbb{R}$ = dimensionless reaction rate
t = time (s)
T = temperature (K)
u = vector of state variables
v = superficial fluid velocity (m/s)
x = conversion (defined by Eq. 11)
z = axial coordinate (m)

Greek letters

β = adiabatic temperature rise (defined by Eq. 11)
ΔH = heat of reaction (J mol^{-1})
ε = bed voidage
ϕ = azimuthal coordinate
γ = dimensionless activation energy (defined by Eq. 11)
η = dimensionless axial coordinate
$\bar{\lambda}$ = effective thermal conductivity (W m^{-1} K^{-1})

μ = transversal eigenmode number
θ = dimensionless temperature (defined by Eq. 3)
Θ_{BL} = fraction of the surface that is blocked
ρ = density (kg m^{-3})
σ = coefficient of imaginary eigenvalue
τ = dimensionless time (defined by Eq. 3)
$\boldsymbol{\omega}$ = eigenvector
$\boldsymbol{\omega}_{mn}$ = transversal perturbation vector (defined by Eq. 19)
ξ = dimensionless radial coordinate
ψ = eigenvalue

Other
$\| \|$ = norm 2

Subscripts
a = axial
BL = blocking
$\perp$ = transversal
f = fluid phase
i = imaginary
in = inlet
m = azimuthal mode number
n = radial mode number
p = particle
r = real
R = reaction
R1 = transversal thermal dispersion
RE = reactivation
s = solid phase
ss = steady state

Superscripts
h = heat
m = mass

Literature Cited

1. Matros YS. Unsteady Processes in Catalytic Reactors. Amsterdam: Elsevier; 1985.
2. Barkelew CH, Gambhir BS. Stability of trickle-bed reactors. *ACS Symp Ser*. 1984;237:61–81.
3. Jaffe SB. Hot spot simulation in commercial hydrogenation orocesses. *Ind Eng Chem Process Des Dev*. 1976;15:410–416.
4. Edwards WM, Worley FL Jr, Luss D. Temperature fluctuations (flickering) of catalytic wires and gauzes—II. Experimental study of butane oxidation on platinum wires. *Chem Eng Sci*. 1973;28:1479–1491.
5. Murtagh MJ, Sherwood DL, Socha LS Jr. Development of a diesel particulate filter composition and its effect on thermal durability and filtration performance. *SAE Trans*. 1994;103:251–261.
6. Wicke E, Onken HU. Periodicity and chaos in a catalytic packed bed reactor for CO oxidation. *Chem Eng Sci*. 1988;43:2289–2294.
7. Wicke E, Onken HU. Bifurcation, Periodicity, and Chaos by Thermal Effects in Heterogeneous Catalysis. From Chemical to Biological Organization; Berlin/New York: Springer-Verlag, 1988;68–81.
8. Marwaha B, Annamalai J, Luss D. Hot zone formation during carbon monoxide oxidation in a radial flow reactor. *Chem Eng Sci*. 2001;56:89–96.
9. Marwaha B, Luss D. Formation and dynamics of a hot zone in a radial flow reactor. *AIChE J*. 2002;48:617–624.
10. Digilov RM, Nekhamkina O, Sheintuch M. Catalytic spatiotemporal thermal patterns during CO oxidation on cylindrical surfaces: experiments and simulations. *J Chem Phys*. 2006;124:34709–34716.
11. Marwaha B, Luss D. Hot zone formation in packed bed reactors. *Chem Eng Sci*. 2003;58:733–738.
12. Marwaha B, Sundarram S, Luss D. Dynamics of transversal hot zones in shallow packed bed reactors. *J Phys Chem B*. 2004;108:14470–14476.
13. Marwaha B, Sundarram S, Luss D. Dynamics of hot zones on top of packed bed reactors. *Chem Eng Sci*. 2004;59:5569–5574.
14. Digilov R, Nekhamkina O, Sheintuch M. Thermal imaging of breathing patterns during CO oxidation on a Pd/glass cloth. *AIChE J*. 2004;50:163–172.
15. Sundarram S, Marwaha B, Luss D. Global coupling induced temperature patterns on top of packed bed reactors. *Chem Eng Sci*. 2005;60:6803–6805.
16. Stroh F, Balakotaiah V. Modeling of reaction induced flow maldistributions in packed-beds. *AIChE J*. 1991;37:1035–1052.
17. Nguyen D, Balakotaiah V. Flow maldistributions and hot spots in down-flow packed bed reactors. *Chem Eng Sci*. 1994;49:5489–5505.
18. Benneker AH, Kronberg AE, Westerterp KR. Influence of buoyancy forces on the flow of gases through packed beds at elevated pressures. *AIChE J*. 1998;44:263–270.
19. Nguyen D, Balakotaiah V. Reaction driven instabilities in down-flow packed bed reactors. *Proc Roy Soc London*. 1995;450:1–21.
20. Balakotaiah V, Christaforatou EL, West DH. Transverse concentration and temperature nonuniformities in adiabatic packed bed catalytic reactors. *Chem Eng Sci*. 1999;54:1725–1734.
21. Yakhnin V, Menzinger M. On transverse patterns in catalytic packed bed reactors. *Chem Eng Sci*. 2001;56:2233–2236.
22. Viswanathan GA, Luss D, Bindal A, Khinast J. Stationary transversal hot zones in adiabatic packed-bed reactors. *AIChE J*. 2005;51:3028–3038.
23. Viswanathan GA, Luss D. Moving transversal hot zones in adiabatic, shallow packed-bed reactors. *AIChE J*. 2006;52:705–717.
24. Sundarram S, Luss D. Dynamics of transversal hot zones in a shallow packed bed reactor during oxidation of mixtures of C_3H_6 and CO. *Ind Chem Eng Res*. 2007;46:1485–1491.
25. Slinko MG, Slinko MM. Self-oscillations of heterogeneous catalytic reaction rates. *Catal Rev Sci Eng*. 1978;17:119–153.
26. Bos ANR, Hof E, Kuper W, Westerterp KR. Behavior of a single catalyst pellet for the selective hydrogenation of ethyne in ethane. *Chem Eng Sci*. 1993;48:1959–1969.
27. Golubitsky M, Schaeffer DG. Singularities and Groups in Bifurcation Theory, Vol. 1. Springer, 1984.
28. Balakotaiah V, Gupta N, West DH. Transport limited pattern formation in catalytic monoliths. *Chem Eng Sci*. 2002;57:435–448.
29. Viswanathan GA. Transversal Temperature Patterns in Packed Bed Reactors. Ph.D. Dissertation. University of Houston, Houston, TX; 2004.
30. Middya U, Luss D. Impact of global interaction on pattern formation on a disk. *J Chem Phys*. 1995;12:5029–5036.
31. Deuflhard P, Hairer E, Zugck J. One-step extrapolation methods for differential–algebraic systems. *J Numer Math*. 1987;51:501–516.
32. Ehrig R, Nowak U, Oeverdieck L, Deuflhard P. Advance extrapolation methods for large-scale differential algebraic problems. In: Bungartz H-J, Durst F, Zenger Chr, editors. High Performance Engineering Computing. Lecture Notes in Computational Science and Engineering, Vol. 8. Munich, Germany: Springer-Verlag 1999; 233.
33. Nowak U, Weimann L. A family of Newton codes for systems of highly nonlinear equations—algorithm, implementation, application. Technical Report TR90-10. Berlin-Darlem, Germany: Konrad-Zuse-Zentrum für Informationstechnik; 1990.
34. Keller HB. Numerical solutions of bifurcation and nonlinear eigenvalue problems. In: Rabinowitz PH, editor. Applications to Bifurcation Theory: Proceedings of an Advanced Seminar. New York, NY: Academic Press; 1977:159.
35. Golubitsky M, Stewart I, Knobloch E. Target patterns and spirals in planar reaction–diffusion systems. *J Nonlinear Sci*. 2000;10:333–354.
36. Palacios A, Gunaratne GH, Gorman M, Robbins KA. Karhunen–Loève analysis of spatiotemporal flame patterns. *Phys Rev E*. 1998;57:5958–5971.
37. Graham MD, Lane SL, Luss D. Proper orthogonal decomposition analysis of spatiotemporal temperature patterns. *J Phys Chem*. 1993;97:889–894.
38. The Mathworks. Statistics Toolbox For use with Matlab®—User's Guide, Ver. 5.0.2. (http://www.mathworks.com/access/helpdesk/help/pdf_doc/stats/stats.pdf) Natick, MA;The Mathworks Inc.; 2005.
39. Sachs M, Hildebrand S, Völkening J, Wintterlin G. Ertl spatiotemporal self-prganization in a surface reaction: From the Atomic to the Mesoscopic Scale. *Science*. 2001;293:1635–1638.
40. Viswanathan GA, Luss D. Model prediction of hot spots formation in shallow adiabatic packed-bed reactor. *AIChE J*. 2006;52:1533–1538.

Appendix A: Condition for the existence of a Hopf Bifurcation

The eigenvalues of $\mathbb{L}$ are the solutions of the characteristic polynomial[40]

$$\det(\mathbb{L}-\psi\mathbb{I}) = -\psi^3 + \mathrm{tr}(\mathbb{L})\psi^2 - \mathrm{prod}(\mathbb{L})\psi + \det(\mathbb{L}) = 0 \quad \text{(A1)}$$

where $\mathbb{I}$ is the identity matrix, $\mathrm{tr}(\mathbb{L})$ is the trace of matrix $\mathbb{L}$, and

$$\det(\mathbb{L}) = \frac{1}{Le}[Da_{\mathrm{BL}}\mathbb{G}_{1\Theta_{\mathrm{BL}}} - Da_{\mathrm{RE}}\mathbb{G}_{2\Theta_{\mathrm{BL}}}](1-\mathbb{R}_x-\beta\mathbb{R}_\theta) + \frac{\beta\mathbb{R}_{\Theta_{\mathrm{BL}}}}{Le}[Da_{\mathrm{BL}}\mathbb{G}_{1\theta} - Da_{\mathrm{RE}}\mathbb{G}_{2\theta}] \quad \text{(A2)}$$

$$\mathrm{tr}(\mathbb{L}) = \left[-1+\mathbb{R}_x - \frac{1}{Le} + \frac{\beta\mathbb{R}_\theta}{Le} + Da_{\mathrm{BL}}\mathbb{G}_{1\Theta_{\mathrm{BL}}} - Da_{\mathrm{RE}}\mathbb{G}_{2\Theta_{\mathrm{BL}}}\right] \quad \text{(A3)}$$

$$\mathrm{prod}(\mathbb{L}) = \left[\frac{1}{Le}(1-\mathbb{R}_x-\beta\mathbb{R}_\theta) - \det(\mathbb{L}) + (Da_{\mathrm{BL}}\mathbb{G}_{1\Theta_{\mathrm{BL}}} - Da_{\mathrm{RE}}\mathbb{G}_{2\Theta_{\mathrm{BL}}})\left(-1+\mathbb{R}_x - \frac{\mathbb{R}_x}{Le}\right)\right] \quad \text{(A4)}$$

A Hopf bifurcation from a uniform steady state of a shallow reactor model occurs when a pair of complex eigenvalues of $\mathbb{L}$ ($\psi = \pm i\sigma$) crosses the imaginary axis. ψ is the solution of

$$\pm i\sigma^3 - \mathrm{tr}(\mathbb{L})\sigma^2 \mp \mathrm{prod}(\mathbb{L})i\sigma + \det(\mathbb{L}) = 0 \quad \text{(A5)}$$

Separating the real and imaginary parts of the above equation, and equating the real part to zero, a unique nontrivial solution of σ exists only if:

$$\det(\mathbb{L}) - \mathrm{tr}(\mathbb{L}) \times \mathrm{prod}(\mathbb{L}) = 0 \quad \text{(A6)}$$

After a sequence of algebraic manipulations, Eq. A6 can be rewritten as

$$\det(\mathbb{L}) = \left[-1+\mathbb{R}_x - \frac{1}{Le} + \frac{\beta\mathbb{R}_\theta}{Le} + Da_{\mathrm{BL}}\mathbb{G}_{1\Theta_{\mathrm{BL}}} - Da_{\mathrm{RE}}\mathbb{G}_{2\Theta_{\mathrm{BL}}}\right] \times \left[\frac{1}{Le}(1-\mathbb{R}_x-\beta\mathbb{R}_\theta) - \det(\mathbb{L}) + (Da_{\mathrm{BL}}\mathbb{G}_{1\Theta_{\mathrm{BL}}} - Da_{\mathrm{RE}}\mathbb{G}_{2\Theta_{\mathrm{BL}}})\left(-1+\mathbb{R}_x - \frac{\mathbb{R}_x}{Le}\right)\right] \quad \text{(A7)}$$

Equation A7 is the condition for the existence of a Hopf bifurcation from a uniform steady state in a shallow packed-bed reactor model.

Appendix B: Stability of Stationary nonuniform States bifurcating from Uniform States

A uniform steady state is stable to homogeneous perturbations if and only if all the eigenvalues of Eq. 16 have a negative real part. A necessary condition for a stable uniform steady state is

$$Le\det(\mathbb{L}) = -(-1+\mathbb{R}_x)W_2 - \beta\mathbb{R}_\theta W_2 + \beta\mathbb{R}_{\Theta_{\mathrm{BL}}}W_1 < 0 \quad \text{(B1)}$$

where $\mathbb{L}$ is the first Fréchet derivative defined in Eq. 16,

$$W_1 = Da_{\mathrm{BL}}\mathbb{G}_{1\theta} - Da_{\mathrm{RE}}\mathbb{G}_{2\theta} \quad \text{(B2)}$$

$$W_2 = Da_{\mathrm{BL}}\mathbb{G}_{1\Theta_{BL}} - Da_{\mathrm{RE}}\mathbb{G}_{2\Theta_{\mathrm{BL}}} = -\left\{\exp\left[\frac{\gamma_{\mathrm{BL}}\theta}{1+\theta}\right] + \exp\left[\frac{\gamma_{\mathrm{RE}}\theta}{1+\theta}\right]\right\} < 0 \quad \forall\gamma_{\mathrm{BL}},\gamma_{\mathrm{RE}},\theta \quad \text{(B3)}$$

A nonhomogeneous perturbation (Eq. 19) of a uniform steady state can lead to a bifurcation to a stationary nonuniform state only when

$$\det(\mathbb{L}-\mathbb{P}) = 0 \quad \text{(B4)}$$

where $\mathbb{P}$ is defined in Eq. 21. Following expansion of the determinant, algebraic manipulation and use of Eq. B1, Eq. B4 can be rewritten as

$$Le\det(\mathbb{L}) - (-1+\mathbb{R}_x)W_2\frac{\mu_{mn}^2}{Pe_\perp^{\mathrm{h}}} - \frac{\mu_{mn}^2}{Pe_\perp^{\mathrm{m}}} \times \left[(-1+\beta\mathbb{R}_\theta)W_2 - \frac{\mu_{mn}^2}{Pe_\perp^{\mathrm{h}}}W_2 - \beta\mathbb{R}_{\Theta_{\mathrm{BL}}}W_1\right] = 0 \quad \text{(B5)}$$

The condition for loss of stability of a uniform state leading to nonuniform states is

$$(1-\mathcal{M}) = \frac{Le\det(\mathbb{L}) - (-1+\beta\mathbb{R}_\theta)W_2\frac{\mu_{mn}^2}{Pe_\perp^{\mathrm{h}}} - \frac{\mu_{mn}^2}{Pe_\perp^{\mathrm{h}}}\left[(-1+\beta\mathbb{R}_\theta)W_2 - \frac{\mu_{mn}^2}{Pe_\perp^{\mathrm{h}}}W_2 - \beta\mathbb{R}_{\Theta_{\mathrm{BL}}}W_1\right]}{Le\det(\mathbb{L}) - (-1+\mathbb{R}_x)W_2\frac{\mu_{mn}^2}{Pe_\perp^{\mathrm{h}}}} \quad \text{(B6)}$$

where $\mathcal{M} = Pe_\perp^{\mathrm{m}}/Pe_\perp^{\mathrm{h}}$. On further simplification of Eq. B6 using Eq. B1, the condition for bifurcation from a uniform steady state to a stationary transversal nonuniform state is

$$\left(Le\det(\mathbb{L}) + W_2\frac{\mu_{mn}^2}{Pe_\perp^{\mathrm{h}}}\right)\left(1+\frac{\mu_{mn}^2}{Pe_\perp^{\mathrm{h}}}\right) = (1-\mathcal{M})\left[Le\det(\mathbb{L}) - (-1+\mathbb{R}_x)W_2\frac{\mu_{mn}^2}{Pe_\perp^{\mathrm{h}}}\right] \quad \text{(B7)}$$

On a stable uniform steady state, the left hand side of Eq. B7 is negative definite as $\det(\mathbb{L}) < 0$ and $W_2 < 0$. In packed-bed reactors, $\mathcal{M} = Pe_\perp^{\mathrm{m}}/Pe_\perp^{\mathrm{h}} > 1$. However, Eq. B7 is satisfied only when $\mathcal{M} < 1$. Therefore an $\mathbb{O}(2)$ symmetry-breaking bifurcation to a stationary transversal nonuniform state cannot occur from a stable uniform state for the realistic case of heat dispersion larger than that of the mass. However, an $\mathbb{O}(2)$ symmetry-breaking bifurcation leading to a stationary transversal nonuniform state may occur from the unstable

uniform branches on which $\det(\mathbb{L}) > 0$. This symmetry-breaking transition from a uniform to a nonuniform state typically is a pitchfork bifurcation.[22] The Jacobian ($\mathbb{L}$) of an unstable uniform steady state may have either

Case 1: one positive real eigenvalue

Case 2: a pair of complex eigenvalues with positive real parts and one negative real eigenvalue

Case 3: a pair of complex eigenvalues with positive real parts and one positive real eigenvalue

In Case 1, an $\mathbb{O}(2)$ symmetry-breaking bifurcation of the uniform states cannot change the sign of the positive real eigenvalue. In Case 2, the $\det(\mathbb{L}) < 0$ and condition B7 cannot be satisfied and hence a bifurcation to a nonuniform state cannot occur. In Case 3, the symmetry-breaking bifurcation cannot cause a transition of the imaginary part of the eigenvalues through zero and also change the sign of their real part from positive to negative. Therefore, a bifurcation in these regions will lead only to unstable stationary transversal nonuniform states. This implies that an $\mathbb{O}(2)$ symmetry-breaking bifurcation from the uniform steady states cannot lead to a stable transversal stationary nonuniform states.

Manuscript received Dec. 5, 2006, and revision received Mar. 16, 2007.